Article

Not peer-reviewed version

On the Profuse Lanthanide Effect on Functional Properties of $0.94Na_{0.5}Bi_{0.5}TiO_3$-$0.06BaTiO_3$ Ceramic

Jacem Zidani , Ilham Hamdi Alaoui , Moneim Zannen , Eriks Birks , Zakaria Chchiyai , Mustapha Majdoub , Bouchaib Manoun , Mimoun El Marssi , Abdelilah LAHMAR *

Posted Date: 7 March 2024

doi: 10.20944/preprints202403.0420.v1

Keywords: Sodium Bismuth Titanate; structural refinement; dielectric properties; ferroelectric properties; piezoelectric properties; Photoluminescence

Article

On the Profuse Lanthanide Effect on Functional Properties of $0.94Na_{0.5}Bi_{0.5}TiO_3$-$0.06BaTiO_3$ Ceramic

Jacem Zidani [1,2], Ilham Hamdi Alaoui [1], Moneim Zannen [2], Eriks Birks [3], Zakaria Chchiyai [4], Mustapha Majdoub [2], Bouchaib Manoun [5,6], Mimoun El Marssi [1] and Abdelilah Lahmar [1]*

[1] Laboratory of Physics of Condensed Matter (LPMC), University of Picardie Jules Verne, Scientific, Pole, 33 rue Saint-Leu, 80039 Amiens Cedex 1, France.
[2] Laboratory of Interfaces and Advanced Materials (LIMA), Faculty of Sciences of Monastir, University of Monastir, Bd. Of the Environment, Monastir 5019, Tunisia.
[3] Institute of Solid-State Physics, University of Latvia, Riga, Latvia
[4] Laboratory of Inorganic Materials for Sustainable Energy Technologies (LIMSET), Mohammed VI Polytechnic University (UM6P), 43150, Benguerir, Morocco
[5] Hassan First University of Settat, FST, Rayonnement-Matière et Instrumentation, S3M, 26000, Settat, Morocco
[6] Materials Science, Energy, and Nano-engineering Department, University Mohammed VI Polytechnic, Ben Guerir, Morocco
* Correspondence: abdel.ilah.lahmar@u-picardie.fr; Tel.: +33-3-22-82-76-91

Abstract: The beneficial effects of Lanthanide incorporation into $0.94Na_{0.5}Bi_{0.5}TiO_3$-$0.06BaTiO_3$ (BNT-BT) matrix on its functional properties were investigated. The conventional solid-state method was used for synthesizing samples. The structural refinement revealed that all samples crystallized in R3c rhombohedral symmetry. Raman spectroscopy study was carried out using green laser excitation and revealed that no clear perceptible variation in frequency is observed. Dielectric measurements unveiled that the introduction of rare earth obstructed the depolarization temperature promoted in BNT-BT with decreasing the diffusive phase transition with increasing the lanthanide size. Only Dysprosium addition showed comparable diffusion constant and dielectric behavior as the unmodified composition. Further; the comparison of the obtained ferroelectric hysteresis and strain-electric field loops revealed that only Dy-phase exhibited interesting properties comparing parent composition. In addition; the incorporation of lanthanides Ln^{3+} into the BNT-BT matrix led to the development of luminescence characteristics in the visible and near infrared regions; depending on the excitation wavelengths. The simultaneous occurrence of photoluminescence and ferroelectric/piezoelectric properties opens up possibilities for BNT-BT-Ln to exhibit multifunctionality in a wide range of applications.

Keywords: sodium bismuth titanate; structural refinement; dielectric properties; ferroelectric properties; piezoelectric properties; photoluminescence

1. Introduction

Piezoelectric materials have become increasingly important in various applications such as sensors, actuators, and transducers. However, lead-based piezoelectric materials pose a significant risk to human health and the environment, which has led to the development of lead-free alternatives. Among these alternatives, $Na_{0.5}Bi_{0.5}TiO_3$ (BNT) based ceramics have gained attention due to their promising piezoelectric properties [1]. BNT ($Na_{0.5}Bi_{0.5}TiO_3$) is classified as a relaxor ferroelectric and has a Curie temperature of TC = 320 ºC as reported in previous works [2,3].

The perovskite structure ABO_3 is occupied by Bi and Na ions in the A-sites. BNT has R3c - rhombohedral structure at room temperature [4]. Ferroelectric materials, which exhibit dielectric and piezoelectric properties, are widely used in high-performance applications. The emergence of perovskite relaxor ferroelectric materials has opened up fresh avenues across diverse sectors such as medical ultrasonics and energy harvesting [5,6]. In particular, the exceptional piezoelectric properties of perovskite relaxor ferroelectric materials make them suitable for acoustic transducers. Therefore,

 doi:10.20944/preprints202403.0420.v1

the development of lead-free piezoelectric ceramics with enhanced electrical and mechanical properties, such as dopant-modified BNT-based ceramics, can lead to the development of new filed of applications [7]. However, the practical application of BNT-based ceramics is limited by their poor electrical and mechanical properties [8]. To overcome these limitations, dopants have been introduced to modify their crystal structure, resulting in enhanced electrical and mechanical properties [9].

As already known, it has been previously noted that the morphotropic phase boundary (MPB) holds significant importance in lead-based solid solutions [10]. This is due to the fact that the reported piezoelectric and dielectric properties are at their highest in close proximity to the MPB region, providing ample opportunities for enhancing their practical application. Likewise, the $Na_{0.5}Bi_{0.5}TiO_3$ -0.06$BaTiO_3$ (BNT-BT) system has gained significant interest due to the presence of MPB situated between the two phases rhombohedral and tetragonal, which occurs near x = 0.06 [11,12]. The addition of BT to NBT at the MPB results in a notable decrease in coercive fields and significant enhancement in piezoelectric properties when compared to pure BNT [8].

Recent studies [13,14] have shown that incorporating lanthanide elements into the 0.94NBT-0.06BT system can improve properties that are linked to the specific rare earth element used [15–18]. The addition of Ln_2O_3 to BNT-BT piezoelectric ceramics not only enhances their ferroelectric and piezoelectric properties but also are responsible for fluorescence. This finding suggests a potential application of these ceramics in fluorescent light-emitting devices. However, current research lacks a comprehensive and systematic examination of how the doping by different lanthanides impacts the ferroelectric, dielectric, field-strain properties, and fluorescence luminescence intensity of BNT-BT ceramics, according to Wu et al. [19].

These findings emphasize the importance of lanthanides in enhancing the properties of 0.94NBT-0.06BT ceramics. The objective of this study is to examine how the addition of Ln_2O_3 influences the structural, dielectric, piezoelectric, optical and ferroelectric Characteristics of 0.94BNT-0.06BT ceramics.

2. Materials and Methods

The BNT and $0.94Na_{0.5}(Bi_{1-x}Ln_x)_{0.5}TiO_3-0.06BaTiO_3$ceramic doped with lanthanides (x = 1%, Ln = Pr, Nd, Eu, Dy), were prepared by the conventional solid-state technique. We used as precursors with high purity such as Na_2CO_3 (99%), Bi_2O_3 (99%), TiO_2 (99.9%), $BaCO_3$ (99.9%), Pr_2O_3 (99%), Nd_2O_3 (99%), Dy_2O_3 and Eu_2O_3 (99%). The powders were weighed and blended based on the stoichiometric ratio, after which they underwent thorough milling in an agate mortar with ethanol. The calcination procedure was carried out at 850 ◦C for 3 hours (heating rate = 300 ◦C/h). Subsequently, the powders underwent further grinding in an agate mortar before being formed into pellets measuring 8 mm in diameter and approximately 1 mm in thickness. Finally, the compressed discs were subjected to sintering at 1100°C for 3 hours, employing the same heating rate.

The structure BNT-BT-Ln was studied at room temperature using a PanAnalytical X'Pert PRO diffractometer (CuKα = 1.5406 Å) between 10° < 2θ < 80°. The data underwent refinement using the Rietveld refinement method with the FullProf software. The dielectric measurements (εT, tanδ and Cp) were performed at different frequencies using an Impedance Analyzer (Agilent 4284A) in the temperature range of 300 – 800 K. The microstructure of the ceramics was studied by scanning electron microscopy device Philips XL30 (SEM). Raman spectra were obtained within the 100–1000 cm-1 range utilizing a micro-Raman spectrometer LABRAM HRT 4600 HR 800 with 633 nm laser excitation. Polarization hysteresis loops were assessed using the Sawyer-Tower technique. The dielectric permittivity measurements were conducted on samples that had been previously poled employing an impedance analyzer - HP precision LCR meter 4284A. Poling was carried out at room temperature with a 1Hz frequency, subjecting the material to a maximum electric field of 75 kV/cm. Luminescence analysis was conducted using photoluminescence spectroscopy (LabRAM HR Evolution) with different laser wavelengths employed for excitation across all synthesized samples.

3. Results

 doi:10.20944/preprints202403.0420.v1

3.1. X-ray diffraction and structural analysis

The phase purity and structural properties of the elaborated perovskite ceramics are examined by powder X-ray diffraction (XRD) and Rietveld method. Figure 1 exhibits the room temperature powder XRD profiles of the synthesized $Na_{0.5}Bi_{0.5}TiO_3$ (BNT), $0.94Na_{0.5}Bi_{0.5}TiO_3$-$0.06BaTiO_3$ (BNT-BT), and Ln-doped $0.94Na_{0.5}Bi_{0.5}TiO_3$-$0.06BaTiO_3$ (BNT-BT-Ln, Ln = Pr^{3+}, Nd^{3+}, Eu^{3+}, Dy^{3+}) perovskite ceramics. From this figure, all the synthesized compounds exhibit similar XRD patterns with sharp and well-defined diffraction peaks, indicating a similar structure for all the elaborated compounds with good crystallization. As shown in Figure 1, all the XRD peaks of different compounds are indexed to the $Na_{0.5}Bi_{0.5}TiO_3$ (BNT) perovskite structure according to JCPDS card number 36-0340, which crystallizes in the rhombohedral system with the space group R3c. Thus, all the synthesized BNT, BNT-BT, and BNT-BT-Ln compounds exhibit the polycrystalline ABO_3-type perovskite structure with R3c rhombohedral distortion.

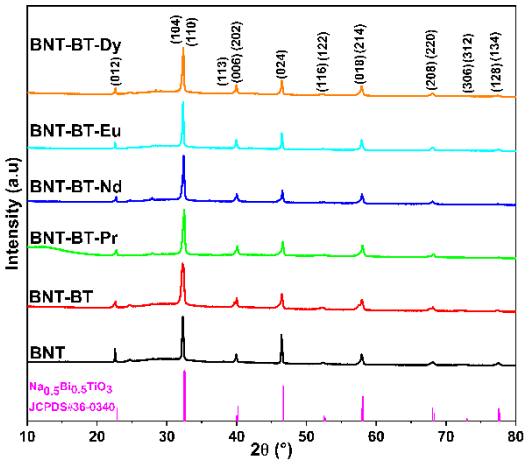

Figure 1. X-ray diffraction profiles of the synthesized BNT, BNT-BT, and BNT-BT-Ln (Ln = Pr^{3+}, Nd^{3+}, Eu^{3+}, Dy^{3+}) perovskite ceramics.

For further investigation and to determine the structural parameters of all the synthesized compositions, their XRD profiles were refined through the Rietveld method employing the Full-prof software. The Rietveld results are shown in Figure 2. The XRD profiles were refined by utilizing a structural model of the BNT phase under the rhombohedral structure and space group R3c as a starting model. However, the XRD peak profiles were determined through the Pseudo-Voigt function. For atomic positions, we consider that the lanthanide ions (Pr^{3+}, Nd^{3+}, Eu^{3+}, Dy^{3+}) occupy A-sites. From Figure 2, all the compositions show good correspondence between experimental intensities (red circles) and calculated intensities (black lines) with small values of R-factors, which prove the R3c rhombohedral symmetry for all the prepared perovskite ceramics. Table 1 displays the refined structural parameters of all synthesized perovskite ceramics. As clearly shown in this table, there is not significant deviation in the values of lattice parameters after doping the BNT-BT sample with different lanthanide ions. Moreover, all lanthanide ions doping induces a small decrease in lattice parameters and volume of the unit cell. This decrement can be explicated by the difference in the ionic radii of the matrix ions ($r_{Na^+} = 1.24$ Å, $r_{Bi^{4+}} = 1.17$ Å, $r_{Ba^{2+}} = 1.47$ Å) and the doping ions ($r_{Pr^{3+}} = 1.179$ Å, $r_{Nd^{3+}} = 1.163$ Å, $r_{Eu^{3+}} = 1.12$ Å, $r_{Dy^{3+}} = 1.083$ Å). Analyzing the ionic radii reveals that the matrix ions (Na^+, Bi^{3+}, and Ba^{2+}) are larger than the doping ions (Pr^{3+}, Nd^{3+}, Eu^{3+}, Dy^{3+}), which leads to a small decrement in lattice parameters.

Table 1. Unit cell parameters (a, c, and V) and the value of tolerance factor (Tf) of the synthesized $Na_{0.5}Bi_{0.5}TiO_3$ (BNT), $0.94Na_{0.5}Bi_{0.5}TiO_3$-$0.06BaTiO_3$ (BNT-BT), and lanthanides-doped (BNT-BT-Ln, Ln = Pr^{3+}, Nd^{3+}, Eu^{3+}, Dy^{3+}) perovskite ceramics.

Sample	BNT-BT-Ln (Ln = Pr^{3+}, Nd^{3+}, Eu^{3+}, Dy^{3+})					
	Structure	Space group	a (Å)	c (Å)	V (Å^3)	T_f

 doi:10.20944/preprints202403.0420.v1

BNT	Rhombohedral structure	$R3c$	5.4991 (2)	13.4367 (9)	351.89 (4)	0.9187
BNT-BT			5.4884 (6)	13.5503 (8)	353.49 (5)	0.9243
BNT-BT-Pr			5.5005 (4)	13.4353 (1)	352.03 (8)	0.9220
BNT-BT-Nd			5.4993 (1)	13.4420 (3)	352.05 (5)	0.9220
BNT-BT-Eu			5.4920 (7)	13.4426 (7)	351.14 (6)	0.9218
BNT-BT-Dy			5.5028 (2)	13.4572 (4)	352.90 (3)	0.9217

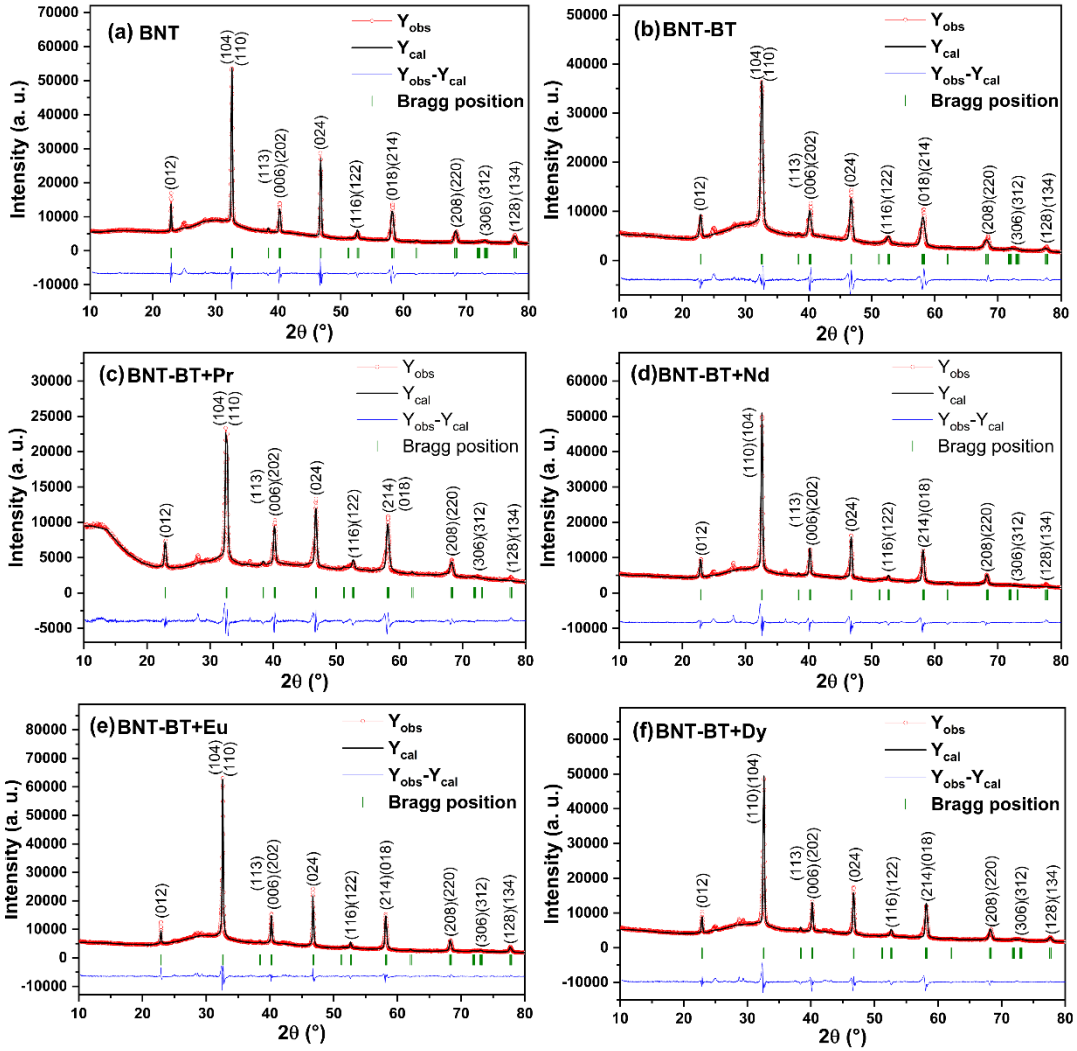

Figure 2. Rietveld refinements of the room temperature powder XRD profiles for the synthesized (a) $Na_{0.5}Bi_{0.5}TiO_3$ (BNT), (b) $0.94Na_{0.5}Bi_{0.5}TiO_3$-$0.06BaTiO_3$ (BNT-BT), and (c-f) lanthanides-doped (BNT-BT-Ln, Ln = Pr^{3+}, Nd^{3+}, Eu^{3+}, Dy^{3+}) perovskite ceramics using the rhombohedral structure with the space group R3c. The red circles and black lines are respectively the experimental and calculated XRD profiles. The blue lines and green bars represent the difference (Y_{obs}-Ycal) and the Bragg position of (hkl) planes, respectively.

The crystal structure of the synthesized perovskites was drawn by VESTA software utilizing the structural parameters acquired from the Rietveld refinement. BNT, BNT-BT, and BNT-BT-Ln perovskites belong to a rhombohedral structure with the R3c space group (N° 161). Figure 3 shows their crystal structure and octahedral distortions under R3c rhombohedral symmetry. In this structure, the Na^+, Bi^{3+}, Ba^{2+}, Pr^{3+}, Nd^{3+}, Eu^{3+}, and Dy^{3+} cations in 12-coordination (green spheres) are located at the Wyckoff 6a site (0, 0, 0.263), and the Ti^{4+} cations (blue spheres) occupy the Wyckoff 6a site (0, 0, 0.006), whereas the O2- anions (red spheres) are placed at the Wyckoff 18b site (0.126, 0.336,

 doi:10.20944/preprints202403.0420.v1

0.083). From Figure 3, it is clearly seen that the TiO_6 octahedra show important distortions, which may be a reason for the ferroelectric behavior.

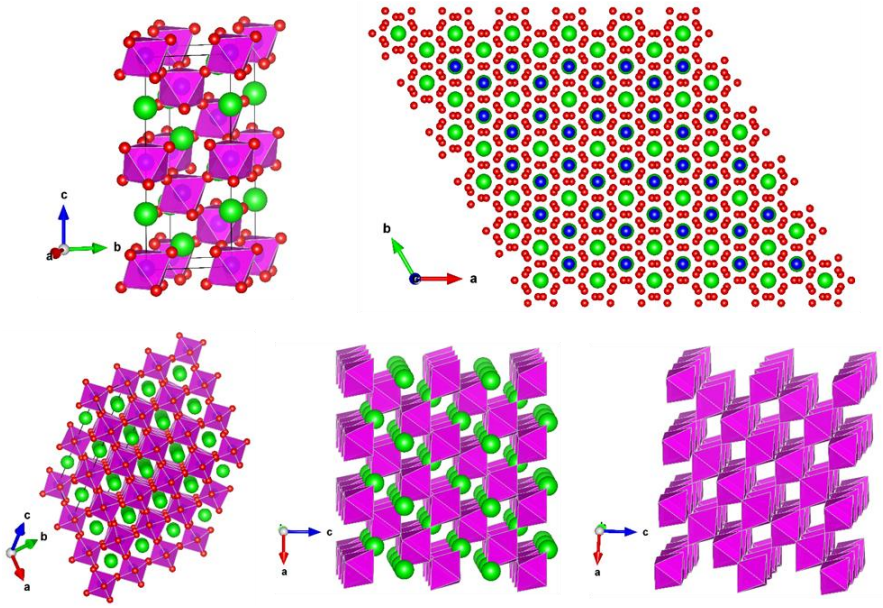

Figure 3. Schematic drawings of crystal structure and octahedral distortions of the synthesized $Na_{0.5}Bi_{0.5}TiO_3$ (BNT), $0.94Na_{0.5}Bi_{0.5}TiO_3$-$0.06BaTiO_3$ (BNT-BT), and lanthanides-doped (BNT-BT-Ln, Ln = Pr^{3+}, Nd^{3+}, Eu^{3+}, Dy^{3+}) perovskite ceramics under rhombohedral structure and space group R3c. Green spheres are used for depicting Na^+, Ba^{2+}, Bi^{3+}, Pr^{3+}, Nd^{3+}, Eu^{3+}, and Dy^{3+} cations located at A-sites, whereas the blue and red spheres represent the Ti^{4+} cations in B-sites and O^{2-} anions, respectively. TiO_6 octahedra are depicted by pink color.

Besides, the stability and the crystal structure of the ABO_3-type perovskite oxide materials can be determined by the tolerance factor (T_f) using the ionic radii of cations (A^{n+}, B^{m+}) and oxygen anion (O^{2-}), as shown in the following equation [20]:

$$T_f = \frac{r_{A^{n+}} + r_{O^{2-}}}{\sqrt{2}(r_{B^{m+}} + r_{O^{2-}})} \quad (1)$$

where, $r_{A^{n+}}$, $r_{B^{m+}}$, and $r_{O^{2-}}$ are the ionic radii of the cations located at A-sites. All the ionic radii were sourced from the R. D. Shannon's ionic radii table [21]. The obtained values of tolerance factor (T_f) for different compounds are listed in Table 1. Generally, for simple perovskites, when the structure is ideal cubic, the value of T_f should be equal to 1. If $T_f > 1$, the structure tends to be tetragonal, and if $T_f < 1$, the structure would be rhombohedral [22]. In our case, all the compounds exhibit a value of T_f smaller than 1, which further confirms the rhombohedral structure for all the synthesized perovskites. However, the addition of lanthanide ions (Pr^{3+}, Nd^{3+}, Eu^{3+}, Dy^{3+}) into the BNT-BT perovskite system led to an insignificant reducing of tolerance factor value from 0.9243 to 0.9217.

Figure 4 shows the SEM micrographs of the prepared ceramics BNT, BNT-BT and BNT-BT-Ln. The synthesized ceramics proved to be relatively dense. The diagram in the inset Figure 4 corresponds to the grain size distribution calculated for the BNT, BNT-BT and BNT-BT-Ln ceramics. With the addition of the lanthanides, it is observed that the average grain size considerably decreases from 5.392 to 0.355μm as shown in Figure 4. according to previous works, the addition of lanthanide elements leads to the inhibition of grain boundary diffusion [23]. The estimated average grain size is around 1.327μm for all the synthesized ceramics. The elemental distributions in BNT-BT and BNT-BT-Ln were scrutinized through Energy Dispersive X-ray (EDX) analysis, as shown in Figure 5. The EDX outcomes validate the existence of all elements in suitable concentrations in prepared ceramic, thereby affirming the efficacy of the synthesis conditions used.

 doi:10.20944/preprints202403.0420.v1

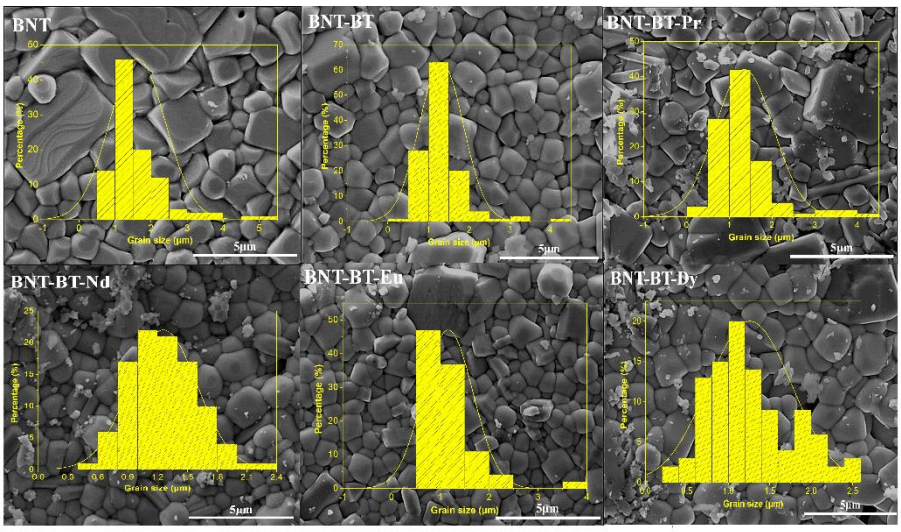

Figure 4. SEM micrographs and Grain size of the synthesized (BNT), (BNT-BT), and lanthanides-doped (BNT-BT-Ln, Ln = Pr^{3+}, Nd^{3+}, Eu^{3+}, Dy^{3+}) perovskite ceramics.

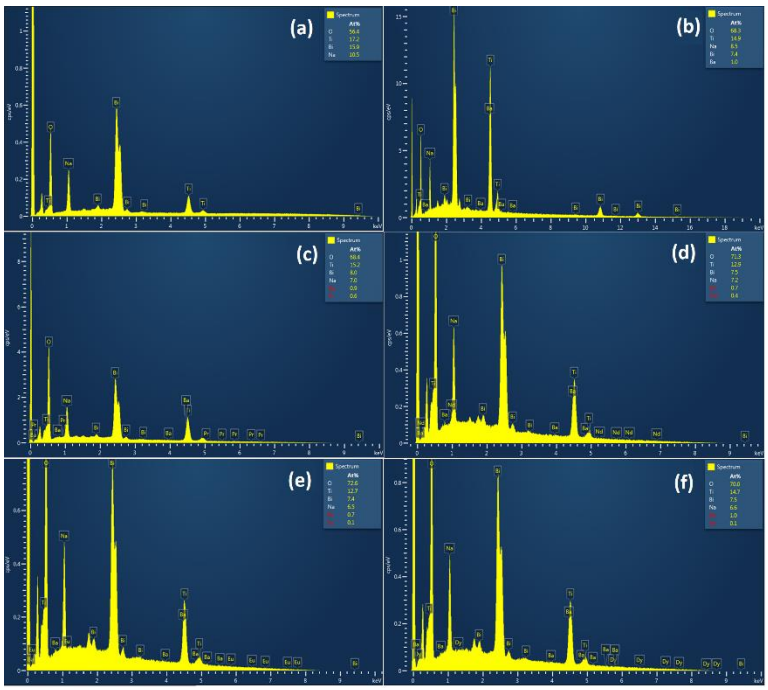

Figure 5. EDX analysis for (a) BNT, (b) BNT-BT, (c) BNT-BT-Pr, (d) BNT-BT-Nd, (e) BNT-BT-Eu, (f) BNT-BT-Dy perovskite ceramics.

3.2. Raman spectra

Raman spectroscopy provides more definitive insights into the microstructure and lattice vibrations of materials [24,25]. Figure 6 depicts the Raman spectrum of the BNT-BT-Ln ceramics, which was acquired on the polished surfaces of the ferroelectric ceramics to mitigate scattering effects. The spectrum of all samples, exhibit broad features due to A-site disorder, which can promote the relaxor nature in ferroelectric materials [26]. According to previous works, the Raman modes of our samples could be grouped into three domains [26]. The first domain is located at feeble wave number region (100-187 cm^{-1}) which is assigned to the vibration of ions from A-site in the structure. It's caused by A-site cation (Na/Bi/Ba/Ln) variations which is very delicate toward phase transitions [27,28]. The second domain near the (187 – 433 cm^{-1}) range, it mainly arises from the internal bending and stretching vibrations of Ti – O bond. Typically, alterations in this region arise not only from the displacement of the polar Ti-cation, but additionally due to octahedral tilt and rotation distortions, which may reflect significant structural variations. This region may be useful for identifying phase

 doi:10.20944/preprints202403.0420.v1

transitions in both classic and complex ferroelectric materials [29]. The last domain is situated between (433–878 cm^{-1}) and belongs to the oxygen and TiO_6 octahedral rotations and vibrations, which are linked from superposition of the transverse optical (TO) and longitudinal optical (LO) bands characterized by A1 with the A1(LO) and E(LO) overlapping bands [30]. All Raman modes exhibit wide modes due to the increase of the disorder by the incorporation of Ba (for BNT-BT) and further by lanthanide element for the rest of samples [31,32].

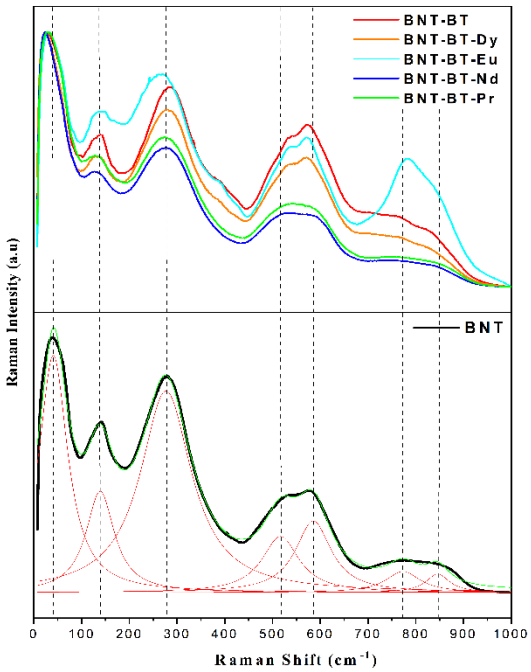

Figure 6. Raman spectra of synthesized ceramics at room temperature with a green laser 532 nm.

It seems that Raman shifts all observed modes did not show any perceptible variation in dependence of added lanthanides, except for the BNT-BT-Eu spectrum where an enhancement of some mode intensity is observed. This phenomenon could be linked to the fluorescence emission of Eu^{3+} in the NBT-BT matrix. It is worth mentioning that the two modes situated between 500 and 600 nm showed a slightly change in their intensities by changing the nature of Lanthanide element, we believe that these octahedra have undergone continuous distortion with increasing the size of rare earth element.

3.3. Dielectric studies

The impact of lanthanide ions (Nd^{3+}, Pr^{3+}, Eu^{3+}, and Dy^{3+}) on the BNT-BT matrix was investigated by the dielectric experiments at different frequencies ranging from 300 to 800 K. Figure 7 displays the changes in the relative permittivity (εr) and dielectric losses (tanδ) of various ceramics with temperature. It is worth noting that the maximum dielectric permittivity value (εr), for BNT and BNT-BT, which is around 3469 and 3237, respectively, is consistent with previous studies [27,33–36].

 doi:10.20944/preprints202403.0420.v1

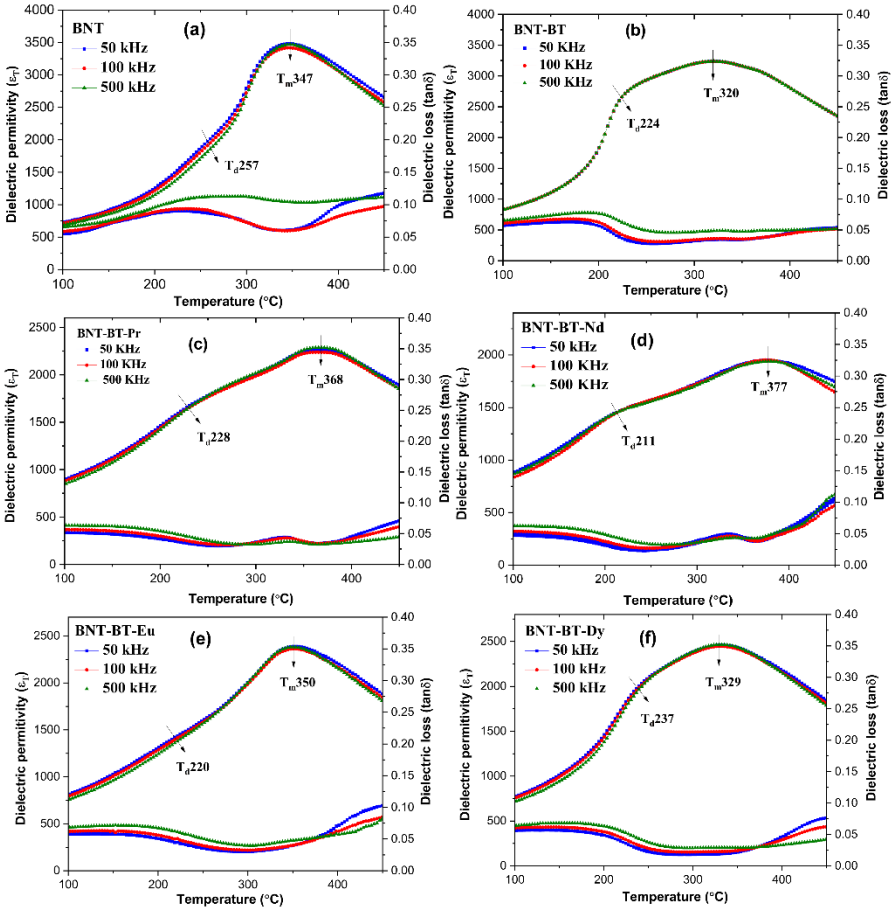

Figure 7. The dielectric constant and loss of (a) BNT, (b) BNT-BT, (c) BNT-BT-Pr, (d) BNT-BT-Nd, (e) BNT-BT-Eu, (f) BNT-BT-Dy.

All the BNT-BT ceramics display two main features of dielectric permittivity [37,38]. The shoulder observed in e(T) at Td indicates the transition from a rhombohedral phase to a modulated phase (R3c + Pnma), characterized by the coexistence of polar nanoregions (PNRs) with (R3c and P4bm) symmetries [39]. This transition was identified using the peak of dielectric loss [40]. The Td has a significant impact on the usefulness of materials in real-world applications. In this study, the Td values observed for all ceramic samples were higher than those reported in previous literature sources [41,42]. The peak in e(T) at Tm corresponds to the transition from tetragonal (P4bm) to most likely orthorhombic (Pnma) [35,43].

It has noted in previous works that the nanodomains with P4bm symmetry contained in the matrix of cubic symmetry contributes to the relaxor type nature in the $Na_{0.5}Bi_{0.5}TiO_3$-$BaTiO_3$ system approaching MPB region [44]. Near Tm, there is no significant peak shift observed at various frequencies. However, these peaks appear broad, indicating a diffuse phase transition. This suggests that the random distribution of Na^+, Bi^{3+}, and Ba^{2+} ions at the A-site in the NBT-BT system is influencing the behavior. is responsible for the diffuse phase transition [37].

The doped samples (BNT-BT-Ln) exhibit a shift in (Tm) towards higher temperatures compared to the NBT-BT, which is attributable to the structural disorder [45]. Because of their small size, lanthanides really cause a significant lattice distortion when they are added to the NBT-BT matrix [46].

It is important to note that the dielectric permittivity of doped compositions at Tm are lower than of the undoped composition. The changes in the dielectric properties are evident in Figure 8, which depicts the evolution of thermal dielectric permittivity at 500 kHz for various samples. It can be observed that the addition of rare earths into the BNT-BT causes significant alterations in these properties.

 doi:10.20944/preprints202403.0420.v1

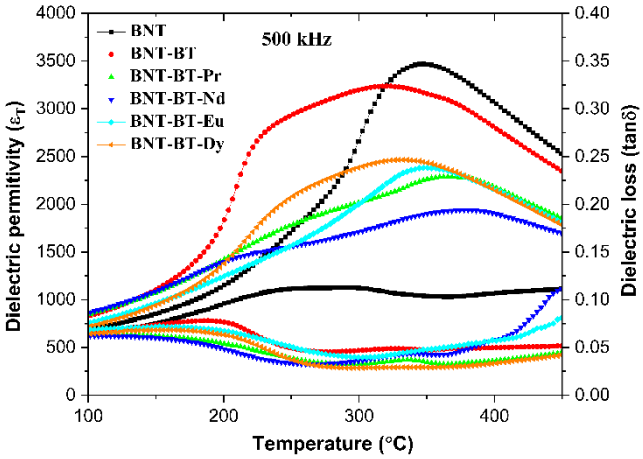

Figure 8. Variation of dielectric permittivity for all samples at 500 kHz as a function of temperature.

From a quantitative standpoint, adding Ln^{3+} to the NBT-BT matrix causes an A-site vacancy to be created in order to maintain charge neutrality [47,48] because of the nonhomogeneous distribution, which impedes the ferroelectric domain barriers from moving and lowers the dielectric permittivity at (Tm).

Figure 9 shows the curves of 1/εr as a function of the temperature at 50 kHz and correspondence with the Curie Weiss law (CW), which generally defines the temperature dependence above ferroelectric-paraelectric phase transition [49]:

$$\frac{1}{\varepsilon_r} = \frac{T - T_{CW}}{C}$$

Noting that εr is the dielectric permittivity, TCW and C are the Curie-Weiss temperature and Curie Weiss constant, respectively. The figure shows three temperature regions, where TM is the maximum permittivity temperature, at which εr (T) start to deviate from linear dependence in direction of lower temperatures (Burns temperature (TB)). The linear part of εr (T) at high temperatures is used to determine the Curie temperature (Tcw) [50]. The degree of deviation from the Curie-Weiss law can be quantified using ΔTM, which is defined as the difference between the Burns temperature (TB) and the temperature of the maximum dielectric constant (TM) [51]. As seen from Figure 9, the values of (TCW) for BNT-BT, BNT-BT-Pr and BNT-BT-Nd ceramics are more deviated from (TM) then for other compositions.

Preprints.org (www.preprints.org) | NOT PEER-REVIEWED | Posted: 7 March 2024 doi:10.20944/preprints202403.0420.v1

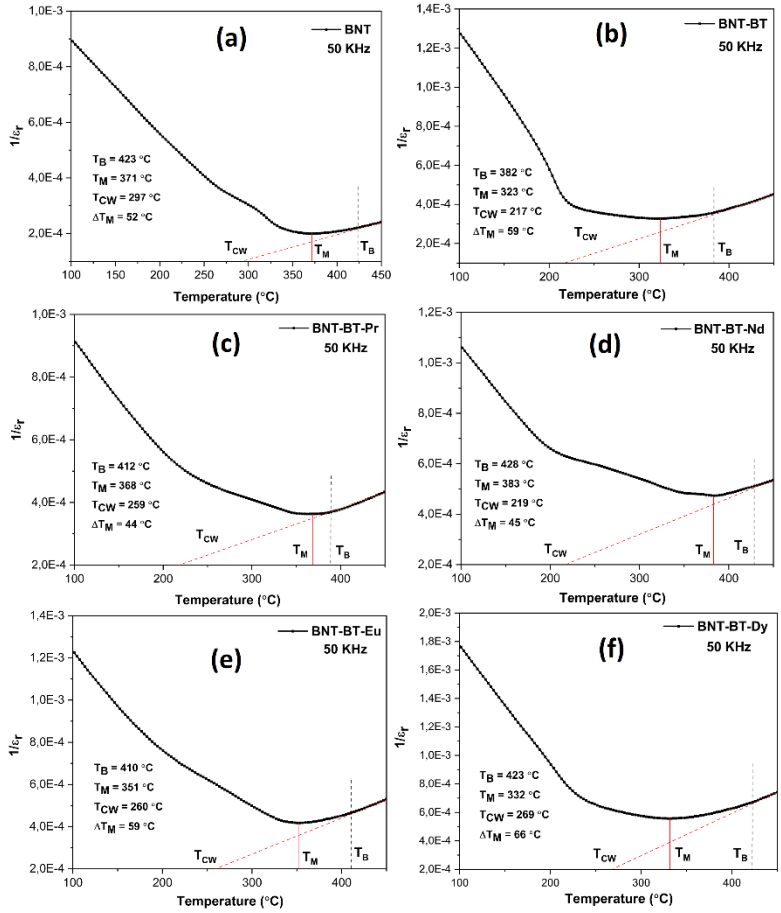

Figure 9. (a) Curve representing the diffusive behavior of (a) BNT, (b) BNT-BT, (c) BNT-BT-Pr, (d) BNT-BT-Nd, (e) BNT-BT-Eu, (f) BNT-BT-Dy ceramics utilizing the inverse of the dielectric permittivity (1/εr) versus temperature.

To assess the degree of diffusivity, the modified Curie-Weiss law can be applied to describe the dielectric behavior of a relaxor ferroelectric:

$$\frac{1}{\varepsilon} - \frac{1}{\varepsilon_m} = \frac{(T - T_m)^\gamma}{C}$$

where ε is the dielectric permittivity at a particular temperature T, εm is the value at Tm, and γ is the diffusivity. C is the modified Curie-Weiss constant.

The diffuse phase transition exhibited by the NBT-BT ceramic is indicative of relaxor behavior tendency [52], which is caused by the coexistence of cations with different valence in equivalent crystallographic sites.

The curve of ln (1/ε-1/εm) as a function of ln (T-Tm) for all samples is displayed in Figure 10. The estimated values of γ were approximately 1.92 for NBT-BT, 1.77, 1.79,1.65 and 1.93 for the samples doped with Pr_2O_3, Nd_2O_3, Eu_2O_3, and Dy_2O_3 respectively, Following the implementation of a linear fit on the experimental data depicted in Figure 10.

 doi:10.20944/preprints202403.0420.v1

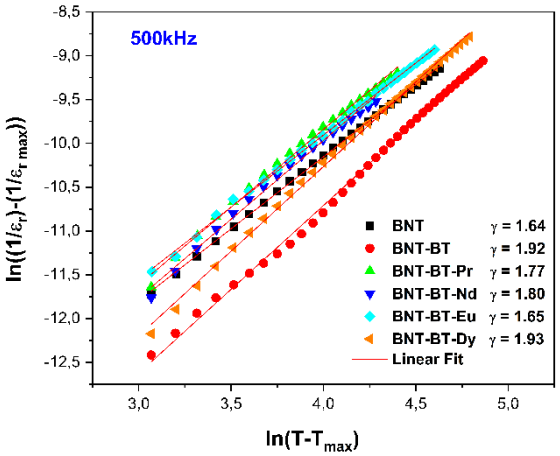

Figure 10. Curve depicting the variation of ln (1/εr - 1/εm) as a function of ln (T - Tm) for the synthesized ceramics.

It's worth mentioning that a material characterized by $\gamma = 1$ is classified as a classical ferroelectric, whereas a standard relaxor ferroelectric exhibits $\gamma = 2$ [53]. The graphs illustrating ln (1/εr - 1/εm) plotted against ln (T-Tm) at 500 kHz for all compositions are shown in Figure 10 demonstrating nearly linear trends with γ values exceeding 1. This suggests that these compositions undergo a diffuse phase transition. The ceramic BNT-BT-Dy exhibited the higher value of γ (above 1.93) compared to the other doped compositions, as shown in Figure 10.

3.4. Ferroelectric performance

In Figure 11, the hysteresis loops of polarization-electric field (P-E) for all samples were analyzed at room temperature at testing frequency of 1Hz. It is evident that all the ceramics exhibit well-saturated ferroelectric hysteresis loops. Pure BNT-BT demonstrates a characteristic P-E loop characterized by a substantial remanent polarization (Pr = 24.7μC/cm²) and coercive field (Ec = 63 kV/cm), aligning well with previously reported findings [54,55].

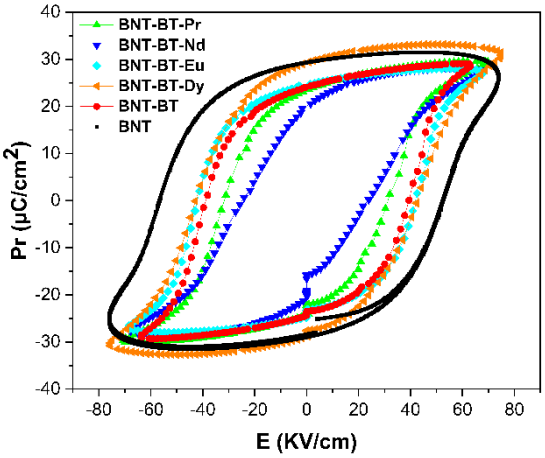

Figure 11. P–E hysteresis loops of all synthesized ceramics at room temperature.

The incorporation of Ln^{3+} elements into the BNT-BT matrix seems to have a notable impact on the characteristics of the hysteresis loop, particularly with regard to remanent polarization (Pr). Upon doping with Dy and Eu element noteworthy alterations in the P-E loop shape were observed, resulting in more inflated loops and a remarkable increase in remanent polarization. Specifically, the remanent polarization value increased from 24μC/cm² for BNT-BT to 29.7μC/cm² for BNT-BT-Dy. In contrast, the BNT-BT-Pr sample exhibited lower remanent polarization value Pr = 20.4μC/cm². The addition of Ln elements in the BNT-BT matrix led to increasing of disorder of the A/B-site cations causing a structural heterogeneity. The diminished ferroelectricity in these samples could potentially

 doi:10.20944/preprints202403.0420.v1

be attributed to the presence of local random fields that disrupt the long-range ferroelectric order. [56]. A summary of various calculated values is presented in Table 2.

Table 2. Evolution of ferroelectric coefficients of BNT-BT, BNT-BT-Ln and BNT.

Samples	Pr (μC/cm²)	E (kV/cm)
BNT	29.5	73.6
BNT-BT	24.7	63
BNT-BT-Dy	29.7	74.8
BNT-BT-Eu	25.1	67.5
BNT-BT-Nd	20.4	67.1
BNT-BT-Pr	23.6	69.8

Figure 12 illustrates the S-E (strain-electric field) loops induced by bipolar electric fields in Ln-BNT-BT ceramics at room temperature. These S-E curves exhibit the classic butterfly shape typicall for ferroelectric materials [57,58].

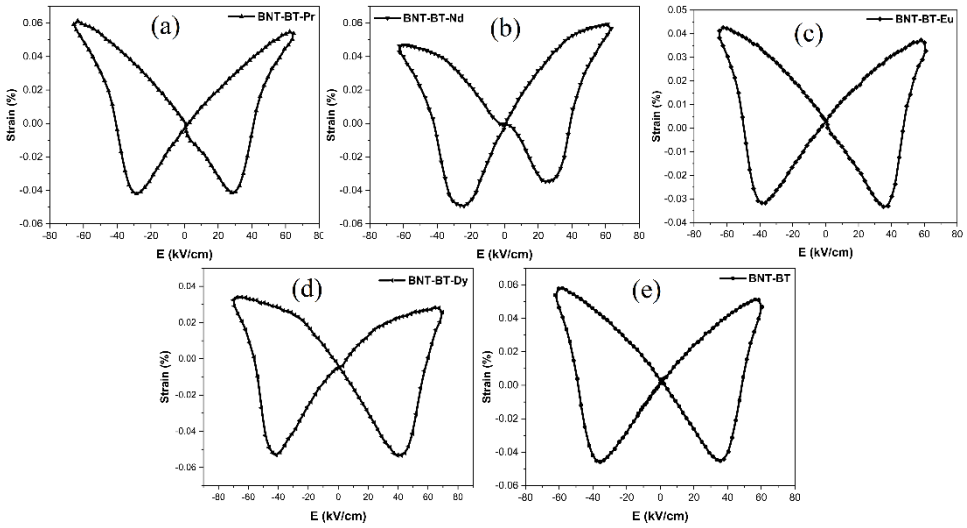

Figure 12. Strain curves of synthesized ceramics: (a) BNT-BT-Pr, (b) BNT-BT-Nd, (c) BNT-BT-Eu, (d) BNT-BT-Dy and (e) BNT-BT.

However, when lanthanides are introduced, this butterfly shape gradually undergoes alterations. Notably, the "positive strain" diminishes progressively, particularly for BNT-BT-Nd, BNT-BT-Eu, and BNT-BT-Dy compositions.

At room temperature, the highest positive strain (Smax) of 0.062% is observed in the case of BNT-BT-Pr, while the most substantial negative bipolar strain of 0.053% is recorded for BNT-BT-Dy. The later can be related with more stable domain structure in field range enough far from Ec. Such assumption is consistent with the observed lower values of dielectric permittivity at room temperature for Dy doped composition.

3.5. Photoluminescence (PL) investigations

The photoluminescence investigation on the BNT-BT-Pr, BNT-BT-Nd, BNT-BT-Eu, and BNT-BT-Dy compounds under various excitation wavelengths is shown in Figure 13.

 doi:10.20944/preprints202403.0420.v1

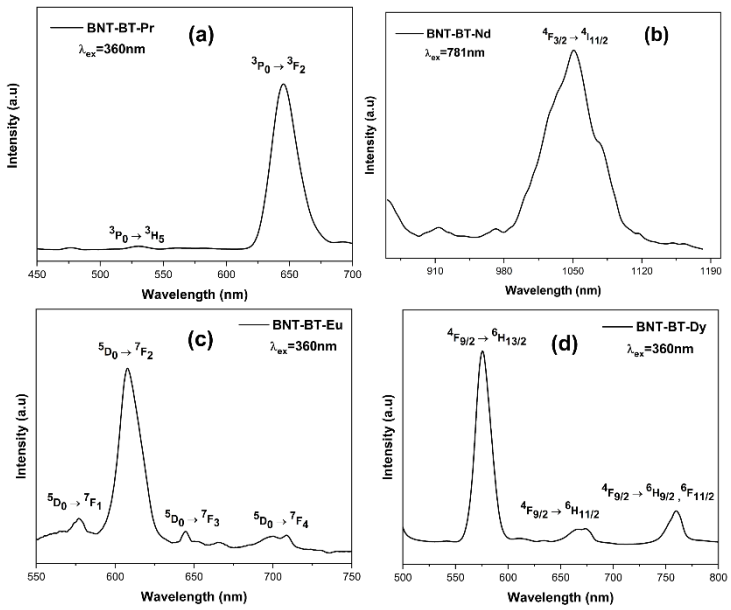

Figure 13. Emission spectra of (a) BNT-BT-Pr, (b) BNT-BT-Nd, (c) BNT-BT-Eu and (d) BNT-BT-Dy samples excited with appropriate wavelengths.

Using a 360 nm laser, the Pr^{3+} doped BNT-BT composition was excited at room temperature. The emission spectra of Pr^{3+} doped BNT-BT exhibit a central red emission at 644 nm, which corresponds to the transitions from $^3P_0 \rightarrow {}^3F_2$, similar to other Pr^{3+} doped perovskite materials [59,60]. The second one, occurring at 530 nm, is associated with the transition $^3P_0 \rightarrow {}^3H_5$, which results in a modest emission of green light. Our results are in agreement with earlier studies [61].

A 781 nm wavelength was used to excite the Nd^{3+} doped BNT-BT ceramic, which then radiated in the near infrared. A prominent band at 1050 nm, which corresponds to the transition of $^4F_{3/2} \rightarrow {}^4I_{11/2}$, is detected in the BNT-BT-Nd spectra (Figure 13). This emission band was also noted in previous publication of Robin et al. [62].

At 360 nm excitation, a prominent red emission peak at 607 nm, which is associated with the $^5D_0 \rightarrow {}^7F_2$ transition, dominates the PL spectra of the BNT-BT-Eu^{3+}. The transitions $^5D_0 \rightarrow {}^7F_1$, $^5D_0 \rightarrow {}^7F_3$, and $^5D_0 \rightarrow {}^7F_4$ are represented by the comparatively feeble emissions with peaks at 576, 644, and 704 nm, respectively [63].

Three distinctive emission peaks at 575 nm, 669 nm, and 760 nm, respectively, are found in the emission spectra of the compound BNT-BT-Dy (Figure 13) and are attributed to the Dy^{3+} transitions $^4F_{9/2} \rightarrow {}^6H_{13/2}$, $^4F_{9/2} \rightarrow {}^6H_{11/2}$ and $^4F_{9/2} \rightarrow {}^6H_{9/2}$, $^6F_{11/2}$ [64]. Our results are well in line with those of Kuzman et al. [65] and Aissa et al. [66].

The chromaticity diagrams based on the "International Commission of Lighting" (CIE) 1931 standards [67], correlated color temperature (CCT) values, and color purity for BNT-BT-Pr, BT-BT-Eu, and BNT-BT-Dy are illustrated in Figure 14. These parameters are crucial for assessing the material's performance in terms of color luminescent emission, particularly in practical applications like light-emitting diodes (LEDs). The CCT values are computed with the CIE 1931 web-based app [68,69] using the McCamy empirical relation [70] and are presented as follows:

$$\mathrm{CCT}\,(x,y) = -449n^3 + 3525n^2 - 6823.3n + 5520.33$$

In the given expression, where $n = \frac{(x-x_e)}{(y-y_e)}$, the coordinates (x, y) represent the color coordinates of a sample, while (x_e = 0.3320, y_e = 0.1858) denote the epicenters of the convergence.

 doi:10.20944/preprints202403.0420.v1

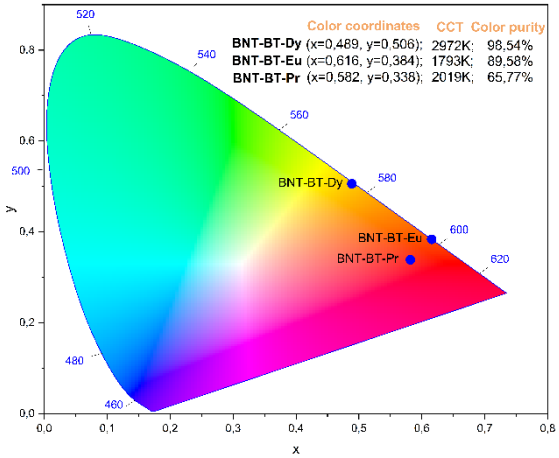

Figure 14. The CIE chromaticity diagram for BNT-BT-Pr, BNT-BT-Eu and BNT-BT-Dy.

The color purity of the emitted color in the BNT-BT-Pr, BNT-BT-Eu, and BNT-BT-Dy systems is determined through the application of the formula provided at [71]:

$$\text{Color purity} = \frac{\sqrt{(x - x_s)^2 + (y - y_s)^2}}{\sqrt{(x_d - x_s)^2 + (y_d - y_s)^2}} \times 100$$

Where:

x and y represent the CIE coordinates of the entire spectrum.

x_s and y_s denote the the CIE coordinates of the standard illuminants of white light.

x_d and y_d stand for the CIE coordinates of the dominant wavelength.

Observing Figure 14, it is evident that the CIE color coordinates for the BNT-BT-Pr, BT-BT-Eu, and BNT-BT-Dy systems (x=0.582, 0.616 and 0.489) are situated comfortably within the red region. The corresponding CCT values are reported as 2019K, 1793K, and 2972K, respectively. Notably, all ceramics exhibit high color purity, making them promising candidates for solid-state lighting applications.

4. Conclusions

$0.94Na_{0.5}Bi_{0.5}TiO_3$-$0.06BaTiO_3$ doped with Ln^{3+} (Pr^{3+}, Nd^{3+}, Eu^{3+}, Dy^{3+}) were prepared using the solid-state technique. Analysis by X-ray diffraction (XRD) confirmed that all samples showed pure phase with rhombohedral R3c symmetry. Scanning electron microscopy (SEM) images demonstrated that the synthesized ceramics were homogeneous and uniform. The temperature dependence of dielectric c permittivity indicated similar transition temperatures, but with some variations in the dielectric constants after incorporating lanthanide elements into the BNT-BT matrix. It seems that the disorder initially present in BNT-BT matrix decrease with increasing the size of lanthanide element. All the examined samples exhibited saturated hysteresis loops that changed with the nature of lanthanide element. It is highlighted in this work that Dy incorporation led to a comparable dielectric behavior as the mother BNT-BT matrix but with improved ferroelectric properties.

Piezoelectric properties have been performed by the mean of strain-electric field; the results demonstrated well-expressed loops of butterfly shape, characteristic for ferroelectric state. Ratio of positive and negative strain vary in dependence of doping element.

Furthermore, the inclusion of Ln^{3+} within the BNT-BT ceramic resulted in distinct light emission in the visible and near infrared regions upon exposure to different excitation wavelengths. The concurrent presence of ferroelectric and optical properties in this system presents considerable potential for optoelectronic applications.

Author Contributions: J.Z.: Investigation, data curation, writing—original draft; I.H.A.: investigation, data curation; M.Z.: visualization, review and editing, validation. E.B.: investigation, review and editing; Z.C.: investigation, data curation; M.M.: validation, supervision; B.M.: writing—review and editing, validation. M.E.M.: visualization, validation; A.L.: conceptualization, writing—review and editing, visualization, validation, supervision. All authors have read and agreed to the published version of the manuscript.

Funding: The authors have not disclosed any funding.

Acknowledgments: Financial support by the project PHC UTIQUE 2022 N° 47593XH is gratefully acknowledged.

Conflicts of Interest: The authors declared that they have no conflict of interest.

References

1. H. Zhang, S. Jiang, K. Kajiyoshi, J. Xiao, Dielectric, Ferroelectric, Pyroelectric, and Piezoelectric Properties of La-Modified Lead-Free Sodium-Potassium Bismuth Titanate Thick Films, J. Am. Ceram. Soc. 93 (2010) 750–757. https://doi.org/10.1111/j.1551-2916.2009.03450.x.
2. M.K. Niranjan, T. Karthik, S. Asthana, J. Pan, U.V. Waghmare, Theoretical and experimental investigation of Raman modes, ferroelectric and dielectric properties of relaxor $Na_{0.5}Bi_{0.5}TiO_3$, J. Appl. Phys. 113 (2013) 194106. https://doi.org/10.1063/1.4804940.
3. H. Nagata, M. Yoshida, Y. Makiuchi, T. Takenaka, Large Piezoelectric Constant and High Curie Temperature of Lead-Free Piezoelectric Ceramic Ternary System Based on Bismuth Sodium Titanate-Bismuth Potassium Titanate-Barium Titanate near the Morphotropic Phase Boundary, Jpn. J. Appl. Phys. 42 (2003) 7401–7403. https://doi.org/10.1143/JJAP.42.7401.
4. S. Kuharuangrong, Effect of La and K on the microstructure and dielectric properties of Bi0.5Na0.5TiO3-PbTiO3, J. Mater. Sci. 36 (2001) 1727–1733. https://doi.org/10.1023/A:1017568424068.
5. P.K. Panda, Review: environmental friendly lead-free piezoelectric materials, J. Mater. Sci. 44 (2009) 5049–5062. https://doi.org/10.1007/s10853-009-3643-0.
6. S. Smail, M. Benyoussef, K. Taïbi, N. Bensemma, B. Manoun, M. El Marssi, A. Lahmar, Structural, dielectric, electrocaloric and energy storage properties of lead free $Ba_{0.975}La_{0.017}(Zr_xTi_{0.95-x})Sn_{0.05}O_3$ (x = 0.05; 0.20) ceramics, Mater. Chem. Phys. 252 (2020) 123462. https://doi.org/10.1016/j.matchemphys.2020.123462
7. S.R. Kanuru, K. Baskar, R. Dhanasekaran, Synthesis, structural, morphological and electrical properties of NBT–BT ceramics for piezoelectric applications, Ceram. Int. 42 (2016) 6054–6064. https://doi.org/10.1016/j.ceramint.2015.12.162.
8. B.-J. Chu, D.-R. Chen, G.-R. Li, Q.-R. Yin, Electrical properties of $Na_{1/2}Bi_{1/2}TiO_3$–$BaTiO_3$ ceramics, J. Eur. Ceram. Soc. 22 (2002) 2115–2121. https://doi.org/10.1016/S0955-2219(02)00027-4.
9. Q. Xu, T. Li, H. Hao, S. Zhang, Z. Wang, M. Cao, Z. Yao, H. Liu, Enhanced energy storage properties of $NaNbO_3$ modified Bi0.5Na0.5TiO3 based ceramics, J. Eur. Ceram. Soc. 35 (2015) 545–553. https://doi.org/10.1016/j.jeurceramsoc.2014.09.003.
10. J.A. Zvirgzds, P.P. Kapostin, J.V. Zvirgzde, T.V. Kruzina, X-ray study of phase transitions in efrroelectric $Na_{0.5}Bi_{0.5}TiO_3$, Ferroelectrics. 40 (1982) 75–77. https://doi.org/10.1080/00150198208210600.
11. T. Takenaka, K.M. Kei-ichi Maruyama, K.S. Koichiro Sakata, $(Bi_{1/2}Na_{1/2})TiO_3$ -$BaTiO_3$ System for Lead-Free Piezoelectric Ceramics, Jpn. J. Appl. Phys. 30 (1991) 2236. https://doi.org/10.1143/JJAP.30.2236.
12. K.R. Kandula, K. Banerjee, S.S.K. Raavi, S. Asthana, Enhanced Electrocaloric Effect and Energy Storage Density of Nd-Substituted 0.92NBT-0.08BT Lead Free Ceramic, Phys. Status Solidi A. 215 (2018) 1700915. https://doi.org/10.1002/pssa.201700915.
13. M. Liu, F. Lei, N. Jiang, Q. Zheng, D. Lin, Enhanced piezoelectricity, bright up-conversion and down-conversion photoluminescence in Er3+ doped $0.94(BiNa)_{0.5}TiO_3$–$0.06BaTiO_3$ multifunctional ceramics, Mater. Res. Bull. 74 (2016) 62–69. https://doi.org/10.1016/j.materresbull.2015.10.008.
14. Q. Li, J. Wang, L. Ma, H. Fan, Z. Li, Large electrocaloric effect in $(Bi_{0.5}Na_{0.5})0.94Ba0.06TiO_3$ lead-free ferroelectric ceramics by La2O3 addition, Mater. Res. Bull. 74 (2016) 57–61. https://doi.org/10.1016/j.materresbull.2015.10.010.
15. C. Zhi-hui, D. Jian-ning, M. Lin, Y. Ning-yi, Z. Yuan-yuan, Piezoelectric and dielectric properties of Dy_2O_3-doped $(Bi_{0.5}Na_{0.5})0.94Ba0.06TiO_3$ lead-free ceramics, J. Alloys Compd. 509 (2011) 482–485. https://doi.org/10.1016/j.jallcom.2010.09.070.
16. D.K. Khatua, A. Agarwal, N. Kumar, R. Ranjan, Probing local structure of the morphotropic phase boundary composition of $Na_{0.5}Bi_{0.5}TiO_3$–$BaTiO_3$ using rare-earth photoluminescence as a technique, Acta Mater. 145 (2018) 429–436. https://doi.org/10.1016/j.actamat.2017.12.022.
17. S.S. Sankaran, Dhanasekaran. R, B. Kumar, Durairajan. A, V. M.A., D.Stephen. L, Study on growth, optical and dielectric properties of 'Nd' DOPED NBT-BT $(0.94(Na_{0.5}Bi_{0.5}TiO_3)$-$0.06BaTiO_3)$ relaxor ferroelectric single crystals, J. Electroceramics. 48 (2022) 143–156. https://doi.org/10.1007/s10832-022-00282-x.
18. M. Zannen, J. Belhadi, M. Benyoussef, H. Khemakhem, K. Zaidat, M. El Marssi, A. Lahmar, Electrostatic energy storage in antiferroelectric like perovskite, Superlattices Microstruct. 127 (2019) 43–48. https://doi.org/10.1016/j.spmi.2018.03.041
19. N. Wu, D. Pang, T. Liang, X. He, Ferroelectric properties and large electric field-induced strain of Eu^{3+} doped $Na_{0.5}Bi_{0.5}TiO_3$–$BaTiO_3$ lead-free ceramics, Ceram. Int. 48 (2022) 23481–23491. https://doi.org/10.1016/j.ceramint.2022.04.343.

20. Z. Chchiyai, F. El Bachraoui, Y. Tamraoui, L. Bih, A. Lahmar, A. Faik, J. Alami, B. Manoun, Synthesis, structural refinement and physical properties of novel perovskite ceramics $Ba_{1-x}Bi_xTi_{1-x}Mn_xO_3$ (x = 0.3 and 0.4), Mater. Chem. Phys. 262 (2021) 124302. https://doi.org/10.1016/j.matchemphys.2021.124302.
21. W. Travis, E.N.K. Glover, H. Bronstein, D.O. Scanlon, R.G. Palgrave, On the application of the tolerance factor to inorganic and hybrid halide perovskites: a revised system, Chem. Sci. 7 (2016) 4548–4556. https://doi.org/10.1039/C5SC04845A.
22. Z. Chchiyai, F. El Bachraoui, Y. Tamraoui, E.M. Haily, L. Bih, A. Lahmar, J. Alami, B. Manoun, Design, structural evolution, optical, electrical and dielectric properties of perovskite ceramics $Ba_{1-x}Bi_xTi_{1-x}Fe_xO_3$ ($0 \le x \le 0.8$), Mater. Chem. Phys. 273 (2021) 125096. https://doi.org/10.1016/j.matchemphys.2021.125096.
23. R. Koduri, L.S. Hermosilla, Effect of Ba on ferroelectric and piezoelectric properties of the PLZT (1.2/55/45) system, Phys. Status Solidi A. 203 (2006) 2119–2127. https://doi.org/10.1002/pssa.200521322.
24. J. Zidani, M. Zannen, M. Hadouchi, H.A.H. Alzahrani, E. Birks, H. Khemakhem, M. Majdoub, M. El Marssi, A. Lahmar, Structural, electrical and optical properties of lanthanide-doped $Na_{0.4}K_{0.1}Bi_{0.5}TiO_3$ ceramics, Phys. B Condens. Matter. 653 (2023) 414680. https://doi.org/10.1016/j.physb.2023.414680.
25. D.Q. Xiao, D.M. Lin, J.G. Zhu, P. Yu, Studies on new systems of BNT-based lead-free piezoelectric ceramics, J. Electroceramics. 21 (2008) 34–38. https://doi.org/10.1007/s10832-007-9087-5.
26. J. Suchanicz, U. Lewczuk, K. Konieczny, Effect of Ba doping on the structural, dielectric and ferroelectric properties of $Na_{0.5}Bi_{0.5}TiO_3$ ceramics, Ferroelectrics. 497 (2016) 85–91. https://doi.org/10.1080/00150193.2016.1163218.
27. K.S.K.R. Chandra Sekhar, Krishnarjun banerjee, S. Asthana, T. Patri, K.C. Mouli, Observation of diffuse relaxor activity and normal thermal stability in Ho – modified NBT – BT lead free ceramics, Ferroelectrics. 568 (2020) 161–174. https://doi.org/10.1080/00150193.2020.1811040.
28. S.A. Nasser, Infrared absorption of some perovskite type titanates containing some additives, J. Mater. Sci. Lett. 9 (1990) 1453–1455. https://doi.org/10.1007/BF00721613.
29. E. Aksel, J.S. Forrester, H.M. Foronda, R. Dittmer, D. Damjanovic, J.L. Jones, Structure and properties of La-modified $Na_{0.5}Bi_{0.5}TiO_3$ at ambient and elevated temperatures, J. Appl. Phys. 112 (2012) 054111. https://doi.org/10.1063/1.4751357.
30. D. Schütz, M. Deluca, W. Krauss, A. Feteira, T. Jackson, K. Reichmann, Lone-Pair-Induced Covalency as the Cause of Temperature- and Field-Induced Instabilities in Bismuth Sodium Titanate, Adv. Funct. Mater. 22 (2012) 2285–2294. https://doi.org/10.1002/adfm.201102758.
31. C. Xu, D. Lin, K.W. Kwok, Structure, electrical properties and depolarization temperature of $(Bi_{0.5}Na_{0.5})TiO_3$–$BaTiO_3$ lead-free piezoelectric ceramics, Solid State Sci. 10 (2008) 934–940. https://doi.org/10.1016/j.solidstatesciences.2007.11.003.
32. R. Selvamani, G. Singh, V. Sathe, V.S. Tiwari, P.K. Gupta, Dielectric, structural and Raman studies on $(Na_{0.5}Bi_{0.5}TiO_3)_{(1-x)}(BiCrO_3)_x$ ceramic, J. Phys. Condens. Matter. 23 (2011) 055901. https://doi.org/10.1088/0953-8984/23/5/055901.
33. P.-Y. Chen, C.-S. Chen, C.-S. Tu, P.-H. Chen, J. Anthoniappen, Effects of texture on microstructure, Raman vibration, and ferroelectric properties in 92.5%$(Bi_{0.5}Na_{0.5})TiO_3$–7.5%$BaTiO_3$ ceramics, J. Eur. Ceram. Soc. 36 (2016) 1613–1622. https://doi.org/10.1016/j.jeurceramsoc.2016.01.038.
34. M. Zannen, A. Lahmar, H. Khemakhem, M. El Marssi, Energy storage property in lead free gd doped $Na_{1/2}Bi_{1/2}TiO_3$ ceramics, Solid State Commun. 245 (2016) 1–4. https://doi.org/10.1016/j.ssc.2016.07.010.
35. M. Benyoussef, M. Zannen, J. Belhadi, B. Manoun, Z. Kutnjak, D. Vengust, M. Spreitzer, M. El Marssi, A. Lahmar, Structural, dielectric, and ferroelectric properties of $Na_{0.5}(Bi_{1-x}Nd_x)_{0.5}TiO_3$ ceramics for energy storage and electrocaloric applications, Ceram. Int. 47 (2021) 26539–26551. https://doi.org/10.1016/j.ceramint.2021.06.068.
36. J. Lv, Q. Li, Y. Li, M. Tang, D. Jin, Y. Yan, B. Fan, L. Jin, G. Liu, Significantly improved energy storage performance of NBT-BT based ceramics through domain control and preparation optimization, Chem. Eng. J. 420 (2021) 129900. https://doi.org/10.1016/j.cej.2021.129900.
37. S. Swain, S. Kumar Kar, P. Kumar, Dielectric, optical, piezoelectric and ferroelectric studies of NBT–BT ceramics near MPB, Ceram. Int. 41 (2015) 10710–10717. https://doi.org/10.1016/j.ceramint.2015.05.005.
38. S.R. Kanuru, K. Baskar, R. Dhanasekaran, Synthesis, structural, morphological and electrical properties of NBT–BT ceramics for piezoelectric applications, Ceram. Int. 42 (2016) 6054–6064. https://doi.org/10.1016/j.ceramint.2015.12.162.
39. M. Benyoussef, M. Zannen, J. Belhadi, B. Manoun, J.-L. Dellis, A. Lahmar, M. El Marssi, Complex impedance and Raman spectroscopy of $Na_{0.5}(Bi_{1-x}Dy_x)_{0.5}TiO_3$ ceramics, Ceram. Int. 46 (2020) 10979–10991. https://doi.org/10.1016/j.ceramint.2020.01.114.
40. O. Turki, A. Slimani, L. Seveyrat, Z. Sassi, H. Khemakhem, L. Lebrun, Enhancement of dielectric, piezoelectric, ferroelectric, and electrocaloric properties in slightly doped $(Na_{0.5}Bi_{0.5})_{0.94}Ba_{0.06}TiO_3$ ceramic by samarium, J. Appl. Phys. 125 (2019) 174103. https://doi.org/10.1063/1.5083670.

41. Q. Zhang, X. Zhao, R. Sun, H. Luo, Crystal growth and electric properties of lead-free NBT-BT at compositions near the morphotropic phase boundary: Crystal growth and electric properties of lead-free NBT-BT, Phys. Status Solidi A. 208 (2011) 1012–1020. https://doi.org/10.1002/pssa.201000052.
42. C. Chen, X. Jiang, Y. Li, F. Wang, Q. Zhang, H. Luo, Growth and electrical properties of $Na_{1/2}Bi_{1/2}TiO_3$–$BaTiO_3$ lead-free single crystal with morphotropic phase boundary composition, J. Appl. Phys. 108 (2010) 124106. https://doi.org/10.1063/1.3516259.
43. Q. Li, J. Wang, L. Ma, H. Fan, Z. Li, Large electrocaloric effect in $(Bi_{0.5}Na_{0.5})0.94Ba0.06TiO_3$ lead-free ferroelectric ceramics by La2O3 addition, Mater. Res. Bull. 74 (2016) 57–61. https://doi.org/10.1016/j.materresbull.2015.10.010.
44. C. Ma, X. Tan, E. Dul'kin, M. Roth, Domain structure-dielectric property relationship in lead-free $(1-x)(Bi_{1/2}Na_{1/2})TiO_3$ $xBaTiO_3$ ceramics, J. Appl. Phys. 108 (2010) 104105. https://doi.org/10.1063/1.3514093.
45. Q. Zhang, T. Yang, Y. Zhang, J. Wang, X. Yao, Enhanced antiferroelectric stability and electric-field-induced strain properties in rare earth-modified $Pb(Zr_{0.63}Sn_{0.26}Ti_{0.11})O_3$ ceramics, Appl. Phys. Lett. 102 (2013) 222904. https://doi.org/10.1063/1.4809934.
46. O. Turki, A. Slimani, N. Abdelmoula, L. Seveyrat, Z. Sassi, H. Khemakhem, L. Lebrun, Lanthanides effects on the ferroelectric and energy-storage properties of $(Bi_{0.5}Na_{0.5})0.94Ba0.06TiO_3$ ceramic: Comparative approach, Solid State Sci. 114 (2021) 106571. https://doi.org/10.1016/j.solidstatesciences.2021.106571.
47. O. Turki, A. Slimani, L. Seveyrat, Z. Sassi, H. Khemakhem, L. Lebrun, Enhancement of dielectric, piezoelectric, ferroelectric, and electrocaloric properties in slightly doped $(Bi_{0.5}Na_{0.5})0.94Ba0.06TiO_3$ ceramic by samarium, J. Appl. Phys. 125 (2019) 174103. https://doi.org/10.1063/1.5083670.
48. F.A. Ismail, R.A.M. Osman, M.S. Idris, Review on dielectric properties of rare earth doped barium titanate, in: Penang, Malaysia, 2016: p. 090005. https://doi.org/10.1063/1.4958786.
49. S. Smail, M. Benyoussef, K. Taïbi, B. Manoun, N. Bensemma, A. Souici, M. El Marssi, A. Lahmar, Structural determination, dielectric and photoluminescence properties of $Ba_{0.975}Ln_{0.017}(Ti_{0.95-x}Zr_xSn_{0.05})O_3$ (Ln = Eu, Ho; x= 0.05, 0.20), Phys. B Condens. Matter 623 (2021) 413365. https://doi.org/10.1016/j.physb.2021.413365.
50. A. Peláiz-Barranco, I. González-Carmenate, F. Calderón-Piñar, Relaxor behaviour in PZN–PT–BT ferroelectric ceramics, Solid State Commun. 134 (2005) 519–522. https://doi.org/10.1016/j.ssc.2005.03.001.
51. M. Aissa, M. Zannen, M. Benyoussef, M. Hadouchi, J. Zidani, J. Belhadi, H.A.H. Alzahrani, M. Majdoub, M. El Marssi, A. Lahmar, Structure, dielectric and ferroelectric Properties of $(1-x)K_{0.5}Na_{0.5}NbO_3$ – $xBi_{0.5}Na_{0.5}TiO_3$ ($0 \leq x \leq 0.1$) Solid Solution, J. Phys. Chem. Solids 185 (2024) 111790. https://doi.org/10.1016/j.jpcs.2023.111790.
52. Q. Xu, M. Chen, W. Chen, H.-X. Liu, B.-H. Kim, B.-K. Ahn, Effect of Ln2O3 (Ln=La, Pr, Eu, Gd) addition on structure and electrical properties of $(Na_{0.5}Bi_{0.5})0.93Ba_{0.07}TiO_3$ ceramics, J. Alloys Compd. 463 (2008) 275–281. https://doi.org/10.1016/j.jallcom.2007.08.068.
53. N.K. Gozuacik, M.C. Bayir, E. Mensur-Alkoy, S. Alkoy, Origin of the Large Field-Induced Strain and Enhanced Energy Storage Response of Rare-Earth-Doped Lead-Free 0.854BNT–0.12BKT–0.026BT Ceramics, IEEE Trans. Ultrason. Ferroelectr. Freq. Control. 68 (2021) 2576–2584. https://doi.org/10.1109/TUFFC.2021.3063146.
54. F. Le Goupil, N.McN. Alford, Upper limit of the electrocaloric peak in lead-free ferroelectric relaxor ceramics, APL Mater. 4 (2016) 064104. https://doi.org/10.1063/1.4950790.
55. W. Jo, S. Schaab, E. Sapper, L.A. Schmitt, H.-J. Kleebe, A.J. Bell, J. Rödel, On the phase identity and its thermal evolution of lead free $(Bi_{1/2}Na_{1/2})TiO_3$-6 mol% $BaTiO_3$, J. Appl. Phys. 110 (2011) 074106. https://doi.org/10.1063/1.3645054.
56. I.H. Alaoui, M. Moussa, N. Lemée, F. Le Marrec, A. Cantaluppi, D. Favry, A. Lahmar, Influence of the Addition of Rare Earth Elements on the Energy Storage and Optical Properties of $Bi_{0.5}Na_{0.5}TiO_3$–$0.06BaTiO_3$ Polycrystalline Thin Films, Materials 16 (2023) 2197. https://doi.org/10.3390/ma16062197.
57. Y. Guo, Y. Liu, R.L. Withers, F. Brink, H. Chen, Large Electric Field-Induced Strain and Antiferroelectric Behavior in $(1-x)(Na_{0.5}Bi_{0.5})TiO_3 - xBaTiO_3$ Ceramics, Chem. Mater. 23 (2011) 219–228. https://doi.org/10.1021/cm102719k.
58. B. Xun, A. Song, J. Yu, Y. Yin, J.-F. Li, B.-P. Zhang, Lead-Free $BiFeO_3$-$BaTiO_3$ Ceramics with High Curie Temperature: Fine Compositional Tuning across the Phase Boundary for High Piezoelectric Charge and Strain Coefficients, ACS Appl. Mater. Interfaces. 13 (2021) 4192–4202. https://doi.org/10.1021/acsami.0c20381.
59. T. Kyômen, R. Sakamoto, N. Sakamoto, S. Kunugi, M. Itoh, Photoluminescence Properties of Pr-Doped $(Ca,Sr,Ba)TiO_3$, Chem. Mater. 17 (2005) 3200–3204. https://doi.org/10.1021/cm0403715.
60. W. Huang, S. He, A. Hao, N. Qin, M. Ismail, J. Wu, D. Bao, Structural phase transition, electrical and photoluminescent properties of Pr^{3+}-doped $(1-x)Na_{0.5}Bi_{0.5}TiO_3$-$xSrTiO_3$ lead-free ferroelectric thin films, J. Eur. Ceram. Soc. 38 (2018) 2328–2334. https://doi.org/10.1016/j.jeurceramsoc.2017.12.057.
61. H. Zhou, X. Liu, N. Qin, D. Bao, Strong red emission in lead-free ferroelectric Pr^{3+}-doped $Na_{0.5}Bi_{0.5}TiO_3$ thin films without the need of charge compensation, J. Appl. Phys. 110 (2011) 034102. https://doi.org/10.1063/1.3611427.

 doi:10.20944/preprints202403.0420.v1

62. I.C. Robin, R. Kumaran, S. Penson, S.E. Webster, T. Tiedje, A. Oleinik, Structure and photoluminescence of Nd:Y_2O_3 grown by molecular beam epitaxy, Opt. Mater. 30 (2008) 835–838. https://doi.org/10.1016/j.optmat.2007.03.003.
63. X. Jiang, X. Jiang, C. Chen, N. Tu, Y. Chen, B. Zhang, Photoluminescence and electrical properties of Eu^{3+}-doped $Na_{0.5}Bi_{4.5}Ti_4O_{15}$-based ferroelectrics under blue light excitation, Front. Mater. Sci. 10 (2016) 31–37. https://doi.org/10.1007/s11706-016-0328-x.
64. R. Yu, D.S. Shin, K. Jang, Y. Guo, H.M. Noh, B.K. Moon, B.C. Choi, J.H. Jeong, S.S. Yi, Photoluminescence Properties of Novel Host-Sensitized Y 6 WO 12 :Dy^{3+} Phosphors, J. Am. Ceram. Soc. 97 (2014) 2170–2176. https://doi.org/10.1111/jace.12937.
65. S. Kuzman, M. Medić, V. Đorđević, I. Zeković, Z. Ristić, L.Đ. Far, M.D. Dramićanin, Luminescence Thermometry Using Dy^{3+}-Activated $Na_{0.25}K_{0.25}Bi_{0.5}TiO_3$ Powders, J. Electron. Mater. 49 (2020) 4002–4009. https://doi.org/10.1007/s11664-020-08109-7.
66. M. Aissa, M. Zannen, H.A.H. Alzahrani, J. Belhadi, Y. Hadouch, D. Mezzane, M. El Marssi, M. Majdoub, A. Lahmar, Multifunctionality of rare earth doped $0.925Na_{0.5}Bi_{0.5}TiO_3$-$0.075K_{0.5}Na_{0.5}NbO_3$ ferroelectric ceramics, J. Alloys Compd. 921 (2022) 166188. https://doi.org/10.1016/j.jallcom.2022.166188.
67. T. Smith, J. Guild, The CIE colorimetric standards and their use, Trans Opt Soc (1931) 73.
68. E H H Hasabeldaim, CIE 1931 web-based app, Zdravookhr. Kirg. (2021). https://sciapps.sci-sim.com/CIE1931.html.
69. E.H.H. Hasabeldaim, H.C. Swart, R.E. Kroon, Luminescence and stability of Tb doped CaF_2 nanoparticles, RSC Adv. 13 (2023) 5353–5366. https://doi.org/10.1039/D2RA07897J.
70. C.S. McCamy, Correlated color temperature as an explicit function of chromaticity coordinates, Color Res. Appl. 17 (1992) 142–144. https://doi.org/10.1002/col.5080170211.
71. Color purity calculator for a luminescence spectrum (1931), (n.d.). https://sciapps.sci-sim.com/color_purity.html.